minerals

MDPI

Article

Laboratory Emissivity Spectra of Sulphide-Bearing Samples, New Constraints for the Surface of Mercury: Oldhamite in Mafic Aggregates

Cristian Carli [1,*], Sabrina Ferrari [2], Alessandro Maturilli [3], Giovanna Serventi [4], Maria Sgavetti [4], Arianna Secchiari [4,5], Alessandra Montanini [4] and Jörn Helbert [3]

[1] National Institute for Astrophysics (INAF), Institute for Space Astrophysics and Planetology, Via Fosso del Cavaliere 100, 00133 Roma, Italy
[2] Department of Geoscience, University of Padova, Via Gradenigo 6, 35131 Padova, Italy; sabrina.ferrari@unipd.it
[3] German Aerospace Center (DLR), Institute for Planetary Research, Rutherfordstraße 23, 12489 Berlin, Germany; alessandro.maturilli@dlr.de (A.M.); joern.helbert@dlr.de (J.H.)
[4] Department of Chemistry, Life Science and Environmental Sustainability, University of Parma, Parco Area delle Scienze, 11/a, 43124 Parma, Italy; giovanna.serventi@gmail.com (G.S.); maria.sgavetti@unipr.it (M.S.); arianna.secchiari@unimi.it (A.S.); alessandra.montanini@unipr.it (A.M.)
[5] Department of Earth Science "A. Desio", University of Milan, Via Botticelli 23, 20131 Milano, Italy
* Correspondence: cristian.carli@inaf.it

Abstract: Exploration of Mercury will continue in the near future with ESA/JAXA's BepiColombo mission, which will increase the number and the type of datasets, and it will take advantage of the results from NASA's MESSENGER (MErcury Surface, Space ENviroment, GEochemistry and Ranging) mission. One of the main discoveries from MESSENGER was the finding of a relatively high abundance of volatiles, and in particular of sulphur, on the surface. This discovery correlates well with the morphological evidence of pyroclastic activity and with features attributable to degassing processes like the hollows. BepiColombo will return compositional results from different spectral ranges and instruments, and, in particular, among them the first results from the orbit of emissivity in the thermal infrared. Here, we investigate the results from the emissivity spectra of different samples between a binary mixture of a volcanic regolith-like for Mercury and oldhamite (CaS). The acquisitions are taken at different temperatures in order to highlight potential shifts due to both mineral variation and temperature dependence on these materials that potentially could be present in hollows. Different absorption features are present for the two endmembers, making it possible to distinguish the oldhamite with respect to the regolith bulk analogue. We show how, in the mixtures, the Christiansen feature is strongly driven by the oldhamite, whereas the Reststrahlen minima are mainly dominated by mafic composition. The spectral contrast is strongly reduced in the mixtures with respect to the endmembers. The variations of spectral features are strong enough to be measured via MERTIS, and the spectral variations are stronger in relation to the mineralogy with respect to temperature dependence.

Keywords: planetary; silicate; sulphide; emissivity; temperature; Mercury

Citation: Carli, C.; Ferrari, S.; Maturilli, A.; Serventi, G.; Sgavetti, M.; Secchiari, A.; Montanini, A.; Helbert, J. Laboratory Emissivity Spectra of Sulphide-Bearing Samples, New Constraints for the Surface of Mercury: Oldhamite in Mafic Aggregates. *Minerals* **2024**, *14*, 62. https://doi.org/10.3390/min14010062

Academic Editors: Kattathu Mathew and Bernard Hubbard

Received: 25 September 2023
Revised: 18 December 2023
Accepted: 28 December 2023
Published: 4 January 2024

1. Introduction

The Hermean surface has been characterized, from a compositional point of view, mainly thanks to some element ratios measured during the MESSENGER mission via XRS (X-ray spectrometer; [1,2]) and GNRS (gamma ray and neutron spectrometer; [3,4]). Visible to near-infrared (VNIR) data, acquired by MESSENGER, show a large variability of spectral properties; however, they do not permit us to retrieve major mineralogical phases. Neither MASCS (Mercury stmospheric and surface composition spectrometer; [5,6]) nor MDIS (Mercury dual imaging system; [7,8]) spectra show diagnostic absorption, with

the exceptions of rimless depressions with flat floors, called hollows, where MDIS colour images can reveal a potential absorption band, with a minimum between 630 and 750 nm. This minimum has been ascribed as related to the presence of either some sulphide, e.g., CaS, MgS or MnS [9,10], or to some iron-free mafic minerals [11] that contain alternative transition elements (e.g., Cr, Ti, Ni).

In particular, the possible presence of sulphide within hollows is intriguing considering that:

> The hollows were morphologically attributed to degassing processes (e.g., [12,13]); relatively unexpected high S/Si has been measured on Mercury's surface (e.g., [1,14]); the surface of Mercury has undergone extensive pyroclastic activity (e.g., [15–18]) which indicates high levels of volatile components in the magma reservoir [19].

In particular, in some specific regions where the level of S/Si is high, Mg/Si and Ca/Si also show higher values, suggesting the possible formation of CaS and MgS phases [1,20]. These sulphides have been observed in reflectance and emittance, suggesting potential spectral variation in the VNIR after different temperature cycles [10], though emissivity spectra of CaS (oldhamite) are not affected by Mercury's surface condition, retaining their characteristic absorption features for both fresh and heated CaS samples [21]. Recently, ref. [22] reported the results about the thermal stability of CaS under Hermean temperature conditions.

The main mineralogy retrieved from elementary information suggests a volcanic composition with variable abundance of plagioclase (oligoclase-andesine), olivine (forsteritic) and pyroxene (enstatitic) (e.g., [23]). This possibly supports the hypothesis that regolith could be mainly characterized by rocks similar to terrestrial magnesian basalts, komatiite or boninite (e.g., [24–26]) with a much lower iron abundance (<1%, e.g., [27,28]) and a relatively higher albite content in plagioclase. The presence of higher iron abundance, or the presence of different transition elements, and/or differences in valence state in silicates, have a direct impact on VNIR spectral properties. In fact, VNIR reflectance properties are strongly influenced by electronic absorptions which often dominate the optical properties. On the other hand, in thermal infrared (TIR) emittance spectra, molecular absorptions provide mineralogical information, whereas transitional elements have a minor impact on Reststrahlen band positions (e.g., [29,30]). These variations do not impact the spectral shape of absorptions which are defined by vibrational processes within the crystal structure (e.g., [31,32]).

Plagioclase TIR spectra can vary from albite to anorthite endmembers [33], whereas the variation is smaller between An20 to An60 [34,35]. Nevertheless, the Na content in plagioclase has been retrieved in [23], taking into account the retrieved high Na_2O (i.e., up to 7%) from [36] which was calculated from the Na/Si reported in [37]. This value has been measured for the north pole with GNRS, at relatively low spatial resolution, and this increase of Na/Si could be related to the migration of Na from the equatorial regions towards the poles [37]. Thus, other regions could have plagioclase with higher Ca composition, but even the retrieved albitic composition of plagioclase on northern lavas could be affected by Na/Si values that are not related to plagioclase [37].

The ongoing ESA/JAXA BepiColombo mission has an onboard VIHI (visible hyperspectral imager, [38], part of the SIMBIO-SYS, Spectrometer and Imaging for MPO Bepicolombo Integrated Observatory SYStem, experiment, [39]), that will acquire imaging data in a larger spectral (0.4–2.0 μm) range with respect to MESSENGER MDIS and MASCS. Moreover, spectral properties of the surface will be investigated using MERTIS (Mercury radiometer and thermal infrared spectrometer, [40]) which will acquire emissivity images in the TIR spectral range (7–14 μm).

The acquisition of spectral data of the surface in the TIR range will permit us to obtain mineralogical information assignable to molecular absorptions and thus recognise the different mineral phases present on the surface of Mercury from the cation–anion and

lattice vibrations of crystalline structures in the middle portion of the electromagnetic spectrum (e.g., [31]).

To support the interpretation of future MERTIS data, in the last decade, emissivity spectra of single mineral phases (e.g., [21,30,41]) as well as spectra of rocks (e.g., [42–44]) were largely investigated at the PSL (Planetary Space Laboratory of DLR, [45]) at variable temperatures. These works highlighted the contribution of temperature variations on driving the shift of specific parameters, like Christiansen feature (CF) and, in particular, some Reststrahlen band absorption minima (RB). Such shifts may mimic variations in composition (e.g., [30]), thus highlighting the importance of taking into account the function of temperature on spectral variations.

Studying controlled and systematic mineral variations can reveal possible trends that can depend both on mineral associations and temperature, but there are few comprehensive studies on emissivity of mineral mixtures. The spectral analysis of mineral mixtures could also provide detection limits of the retrieved minerals. Recently, ref. [46] explored the variation of emissivity features of binary mixtures of plagioclase and clinopyroxene that underwent different temperatures. The authors show how the CF tends to shift to higher wavenumbers with increasing temperature and to lower wavenumbers with decreasing polymerization. Moreover, with increasing temperatures, the RBs shift their position and deepen with respect to CF emissivity, and at high temperatures the plagioclase's higher-wavenumber RBs are not detected. This makes the plagioclase detection in that spectral range more complicated. At lower wavenumbers, a correlation between the pyroxene content and a specific absorption was observed, suggesting that shifts are driven by the pyroxene, which has higher expansion coefficient with respect to that of the plagioclase.

In this manuscript, we investigate the TIR spectral properties of the mineral mixture of a Mg-rich gabbronorite, representing a potential mafic mineralogy in terms of pyroxene-olivine-plagioclase abundances, and CaS, which could be a possible sulphide associated to the degassing processes on Mercury.

2. Methods

2.1. Selection and Preparation of the Samples

We prepared two different endmembers:

A mafic analogue represented by a Mg-gabbronorite (hereafter Mg-GN) from [47] mainly constituted by plagioclase (~62 vol.%), clinopyroxene (~16 vol.%), orthopyroxene (~11 vol.%) and olivine (~11 vol.%), with the mafic mineralogy being particularly Mg-rich; this sample was already used as mafic endmember mixed with graphite for VNIR reflectance acquisitions [48].

CaS has already been used in VNIR [10] and in MidIR [21] acquisitions as a potential Mercury analogue, as suggested from X-Ray (e.g., [1]) and VNIR data (e.g., [9,11]); CaS was chosen because, among the suggested sulphides, it remained stable on Mercury's surface conditions [21,22].

Samples were reduced to <63 μm grainsize via multiple steps of sieving, in order to limit the amount of very fine sized (e.g., <5–10 μm) particles in the powder.

We produced 3 different mixtures, weighing the abundance of the two endmembers, Mg-GN and CaS, in 80%–20%, 60%–40% and 40%–60%, respectively, and preparing 3 g. per sample for emissivity measurements. This sample preparation was carried out at the Sample Preparation Facility at IAPS-INAF.

Sample cups were then prepared at the PSL a week in advance and placed in a desiccator cabinet.

2.2. Experimental Setup

Emissivity spectral measurements were performed at the PSL using a Bruker Vertex 80 V FTIR spectrometer. The set-up operates under low vacuum, with a liquid nitrogen-cooled HgCdTe detector and KBr beam splitter. Emissivity spectra were acquired between 9996 and 400 cm^{-1} at a spectral resolution of 4 cm^{-1}. We then worked in the 2000–700 cm^{-1}-range

(5–14 μm), which is the most promising for diagnostic spectral features. The emissivity spectra of CaS were compared to data from [21] to investigate possible differences which could suggest sample's weathering during the time. The spectra show negligible variations.

An externally evacuated planetary simulation chamber was used to measure emissivity (see [46] and references therein). Samples were heated once, and emissivity was measured under low vacuum at 0.7 mbar in subsequent steps at 375 K, 475 K, 575 K and 675 K. The cup height exceeded the sample height, ensuring more efficient heating and reducing the sample thermal gradients. For each measured sample, the final spectrum was a 256 averaged datum. To calibrate the emittance the calibration body (CB hereafter) was heated and measured at the same temperatures of the sample.

The sample radiance, $I_{(T),}$ and the CB radiance, $CB_{(T),}$ were collected at each scheduled step of temperature. For each sample, 5 scans were averaged to produce a single spectrum. The absolute emissivity of the sample $\varepsilon_{a(T)}$ was derived using the $\varepsilon_{a(T)} = I_{(T)}/CB_{(T)} \cdot E_{CB}$, where E_{CB} is the calibration body emissivity curve. More details regarding the calibration technique are discussed in [41].

2.3. Analytical Approach

Here, we describe the influence of the simulated environment on the measured spectra in terms of wavenumber position of the more diagnostic features and in terms of their spectral contrast.

We identified here different spectral signatures for the two endmembers in the 700–2000 cm^{-1} range. Then, since it is known that, in particular, in the 700–1400 cm^{-1} range, the Christiansen feature (CF) wavenumber and the spectral contrast between CF and the first group of absorption bands is strongly affected by thermal gradients occurring at the shallower radiative depths (see [46]), we concentrated in this range the spectral analysis.

In addition to the CF, the following emissivity minima are considered diagnostic parameters: (i) Reststrahlen bands (hereafter referred as RB) attributable to Si-tetrahedral fundamental vibrations [49] and (ii) transparency features (hereafter referred to as TF) caused by the volume scattering characteristic of fine particle sizes [50]. RBs have long been identified as diagnostic of composition (e.g., [49]) and their frequencies are unaffected by thermal gradients.

Since measurements do not show any evident TF, we just consider CF and RBs positions numbered following the Mg-GN order from highest to lowest wavenumber, as well as the spectral contrast (SC or relative intensity) between the CF and RBs minima, similarly to [46]. Those parameters are discussed with respect to the temperature variation and function of the Mg-GN (mafic endmember) content.

3. Results

At 375 K, the mafic endmember Mg-GN showed the maximum emissivity, i.e., the CF, at 1229 cm^{-1}, consistent with the bulk mafic composition ([51], and references therein) of this sample (see Figure 1, black line, and Table 1, where the data for the lowest temperature, 375 K, are summarized). The RB absorption was composed of 5 different minima of emissivity at 1113, 1001, 959, 928 and 876 cm^{-1}, hereafter indicated as RB0, RB1, RB2, RB3 and RB4, respectively. RB0 was only evident in the Mg-GN endmember (see Table 1), whereas all of the other minima were evident for all the mixtures (see Figures 1 and 2). Additionally, we report the presence of two other maxima (dark blue thin arrows in Figure 1) at ~1080 cm^{-1} and at 780 cm^{-1}, which enclose the RB from 1 to 4.

The other endmember, CaS, instead showed a maximum in emissivity at 1099 cm^{-1} (CF, Table 1), reported also as 9.1 μm in [21]. This mineral phase showed three absorptions at 1038, 885 and 837 cm^{-1}, reported hereafter as RB1*, RB4* and RB5, respectively (see Figure 2, bottom plot). RB1* and RB4* are very close to mafic minima RB1 and RB4, and so in the mixtures, their parameters will be compared to the mafic minima. In Tables 2 and 3, we reoprt the data at different of temperatures, for band position, emissivity and band contrast.

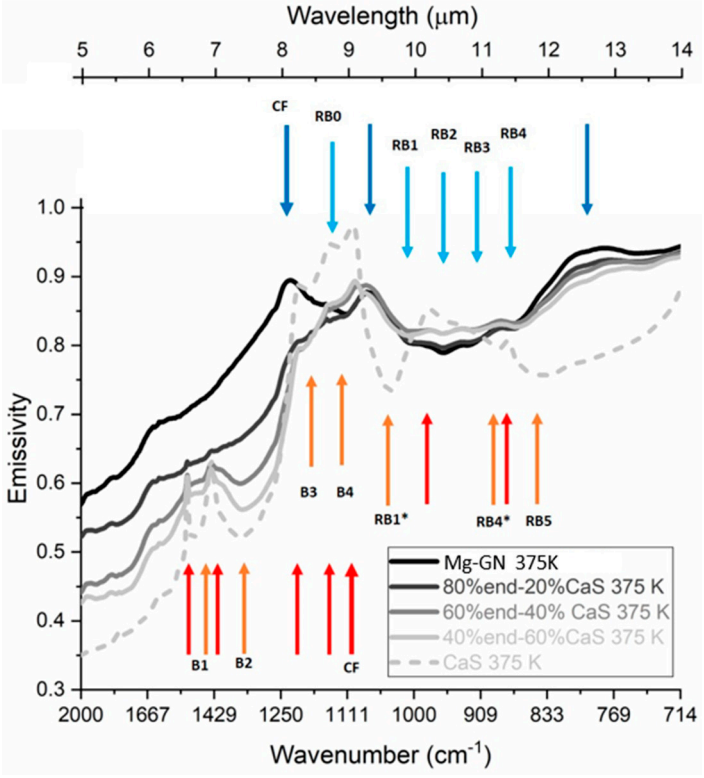

Figure 1. Emissivity spectra of the different samples at lower temperature (375 K). Blue and cyan arrows indicate maxima and minima of Mg-GN endmember, respectively; red and orange arrows indicate maxima and minima of CaS, respectively. See text for more details on absorptions.

Table 1. Position of CF (cm^{-1}) and RBs (cm^{-1}) of emissivity spectra collected at 375 K. Error in position is attributable to spectral resolution, and it is ± 2 cm^{-1}.

Sample	CF	RB0	RB1	RB2	RB3	RB4	RB1*	RB4*	RB5
Mg-gabbronorite (Mg-GN)	1229	1113	1001	959	928	876	--	--	--
20% CaS	1076	--	1001	959	924	872	--	--	--
40% CaS	1078	--	1005	959	920	870	--	--	--
60% CaS	1097	--	1009	959	916	868	--	--	--
CaS	1099	--	--	--	--	--	1038	885	833

nb: -- means no data.

In Figure 1, we also highlighted the presence of two well-defined peaks at 1510 and 1430 cm^{-1}, respectively. The next absorptions, at slightly lower wavenumbers, are indicated as B1 and B2. This portion of the spectral range has not been considered in previous works, though they show specific features of CaS. The maxima (peaks, Max B1 and Max B2 in Table 4), in particular, rose even with a low quantity of sulphides in the mixture (20% of sulphides, dark grey in Figure 1), though they were superimposed by the mafic background already at 60% sulphides, as indicated by the mafic wide weak peak around 1600 cm^{-1}. Nevertheless, they occurred at wavenumbers higher than those covered by MERTIS, so we will not discuss the different temperatures in the rest of the manuscript.

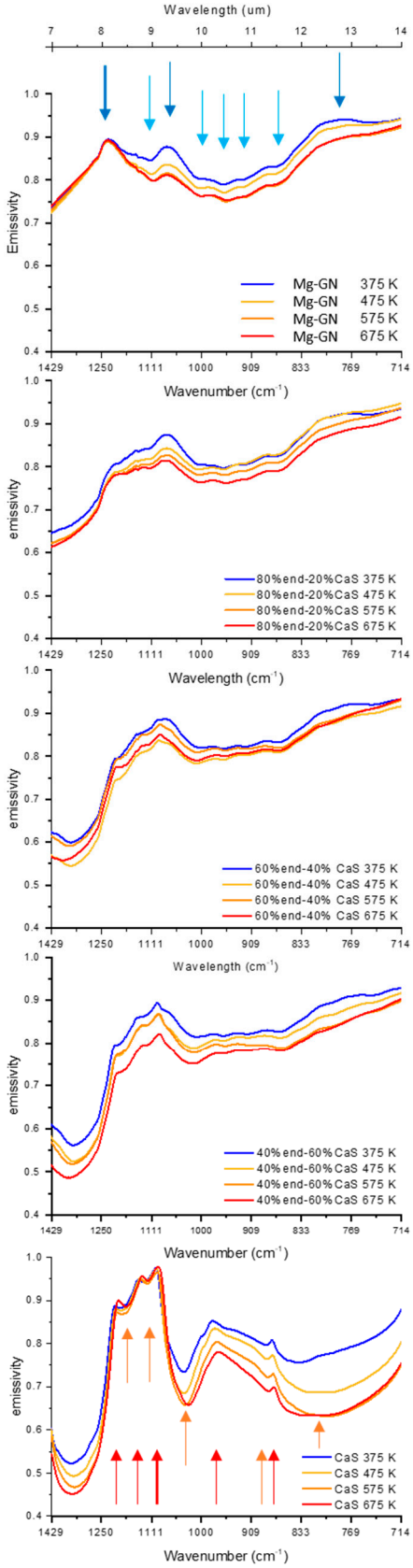

Figure 2. Emissivity spectra of the different samples. From top to bottom Mg-GN; 20% CaS; 40% CaS; 60% CaS. Blue and cyan arrows (labeled in Figure 1) on top plot indicate maxima and minima of Mg-GN, respectively; red and orange arrows on bottom plot indicate maxima and minima of CaS, respectively. See text for more details on absorptions.

Table 2. Position of CF (cm^{-1}) and RBs (cm^{-1}) of emissivity spectra collected at 475 K, 575 K and 675 K. Error in position is attributable to spectral resolution, and it is ± 2 cm^{-1}.

Sample	Temperature (K)	CF	RB0	RB1	RB2	RB3	RB4	RB1*	RB4*	RB5
Mg-gabbronorite (Mg-GN)	475	1230	1111	1003	957	926	876	--	--	--
	575	1230	1107	1003	953	924	876	--	--	--
	675	1230	1105	1003	951	922	876	--	--	--
20% CaS	475	1074	--	1005	959	926	874	--	--	--
	575	1074	--	1005	955	924	874	--	--	--
	675	1076	--	1003	953	920	874	--	--	--
40% CaS	475	1092	--	1011	959	920	868	--	--	--
	575	1090	--	1009	955	916	868	--	--	--
	675	1090	--	1009	955	920	868	--	--	--
60% CaS	475	1095	--	1014	959	914	866	--	--	--
	575	1094	--	1014	955	910	862	--	--	--
	675	1092	--	1018	957	914	864	--	--	--
CaS	475	1099	--	--	--	--	--	1038	883	820
	575	1097	--	--	--	--	--	1034	883	794
	675	1085	--	--	--	--	--	1026	881	804

nb: -- mean no data.

Table 3. Emissivity values and relative intensity (SC) of CF and RBs of spectra collected at 375 K, 475 K, 575 K and 675 K.

Sample	Temperature (K)	CF	RB1	RB2	RB3	RB4	RB1*	RB4*	SC_{RB1}	SC_{RB2}	SC_{RB3}	SC_{RB4}	SC_{RB1*}	SC_{RB4*}
Mg-gabbronorite (Mg-GN)	375	0.895	0.803	0.789	0.800	0.830	--	--	0.092	0.105	0.094	0.065	--	--
	475	0.891	0.781	0.771	0.783	0.813	--	--	0.110	0.120	0.107	0.078	--	--
	575	0.889	0.763	0.750	0.759	0.786	--	--	0.126	0.139	0.130	0.103	--	--
	675	0.893	0.763	0.753	0.761	0.789	--	--	0.130	0.140	0.131	0.104	--	--
20% CaS	375	0.875	0.805	0.797	0.805	0.824	--	--	0.071	0.078	0.071	0.051	--	--
	475	0.843	0.794	0.794	0.806	0.827	--	--	0.049	0.049	0.036	0.016	--	--
	575	0.827	0.781	0.780	0.790	0.808	--	--	0.046	0.046	0.037	0.018	--	--
	675	0.815	0.764	0.762	0.770	0.789	--	--	0.051	0.053	0.045	0.026	--	--
40% CaS	375	0.887	0.821	0.817	0.823	0.832	--	--	0.067	0.070	0.064	0.055	--	--
	475	0.837	0.783	0.792	0.802	0.809	--	--	0.054	0.045	0.035	0.028	--	--
	575	0.874	0.809	0.814	0.818	0.819	--	--	0.065	0.060	0.057	0.055	--	--
	675	0.850	0.790	0.801	0.808	0.814	--	--	0.060	0.050	0.043	0.037	--	--
60% CaS	375	0.894	0.814	0.817	0.822	0.827	--	--	0.079	0.077	0.072	0.067	--	--
	475	0.868	0.788	0.806	0.813	0.813	--	--	0.080	0.063	0.055	0.056	--	--
	575	0.869	0.777	0.794	0.794	0.788	--	--	0.091	0.075	0.074	0.081	--	--
	675	0.822	0.751	0.776	0.783	0.782	--	--	0.071	0.046	0.039	0.040	--	--
CaS	375	0.975	--	--	--	--	0.734	0.796	--	--	--	--	0.241	0.179
	475	0.974	--	--	--	--	0.685	0.764	--	--	--	--	0.289	0.210
	575	0.965	--	--	--	--	0.658	0.722	--	--	--	--	0.307	0.243
	675	0.978	--	--	--	--	0.658	0.690	--	--	--	--	0.320	0.288

nb: -- mean no data.

Table 4. Position of other features attributable to CaS at wavenumber greater than CF. Error in position is attributable to spectral resolution, and it is ± 2 cm^{-1}.

		Max B1 (cm^{-1})	Min B1 (cm^{-1})	Max B2 (cm^{-1})	Min B2 (cm^{-1})	Max B3 (cm^{-1})	Min B3 (cm^{-1})	Max B4 (cm^{-1})	Min B4 (cm^{-1})
20 %CaS	375	1516	1508	1435	1427	1209	1200	1151	1119
	475	1514	1508	1431	1421	1205	1196	1136	1115
	575	1508	1502	1431	--	1203	1192	1126	1121
	675	1506	1502	1427	--	1200	1194	1130	1117
40 %CaS	375	1516	1504	1437	1354	1209	1203	1149	1121
	475	1514	1453	1435	1354	1203	1196	1136	1117
	575	1510	1493	1435	1356	1198	1194	1132	1117
	675	1508	1501	1431	1379	1202	1192	1130	1115

Table 4. *Cont.*

		Max B1 (cm^{-1})	Min B1 (cm^{-1})	Max B2 (cm^{-1})	Min B2 (cm^{-1})	Max B3 (cm^{-1})	Min B3 (cm^{-1})	Max B4 (cm^{-1})	Min B4 (cm^{-1})
60 %CaS	375	1516	1504	1437	1346	1207	1203	1148	1136
	475	1514	1497	1435	1342	1202	1198	1136	1128
	575	1510	1483	1435	1350	1200	1196	1134	1124
	675	1510	1493	1433	1358	1200	1194	1132	1122
CaS	375	1516	1499	1439	1354	1209	1196	1144	1128
	475	1514	1489	1437	1342	1205	1194	1140	1124
	575	1512	1483	1435	1340	1202	1190	1136	1121
	675	1508	1481	1431	1348	1200	1178	1134	1121

nb: -- mean no data.

Two absorptions (B3 and B4) were also present at ~1200 and 1120 cm^{-1}, at wavenumbers higher than the CaS CF but lower than the mafic CF and closer to the weak RB0.

The CF and the absorption minima positions of emissivity spectra collected at 475, 575 and 675 K are listed in Table 2. Diagnostic features of measured emissivity spectra are listed in terms of CF locations and absorption-band minima positions. In Table 3, we report the spectral contrast of each absorption with respect to the emissivity of the CF.

Figure 2 shows the variation of emissivity in the spectral range from 1429 to 714 cm^{-1} for each sample at different temperatures. The emittance at the CF of the two endmembers was coincident for all the different temperatures (see Table 3 and Figure 2). Likewise, the CF position did not shift for Mg-GN (see Tables 1 and 2 and Figure 2), whereas for CaS a shift at lower wavenumber from 1099 to 1085 cm^{-1} moving from 375 K to 675 K was observed. With increasing temperature, both endmembers showed a decrease of emissivity at wavenumbers lower than CF. All the mixtures showed a decrease of emittance from the lower temperature up to higher temperature for the entire spectral range (see Figure 2 and Table 3).

Moreover, we detected a shift of the CF at wavenumbers closer to those of the CaS endmember (evident also in Figure 1 for 375 K, Figure 2 for the other temperatures and in Figure 3) for all the mixtures. In particular, the CF of the 20% CaS sample was at a lower wavenumber with respect to that of the sulphide endmember. In contrast, with an increase of the CaS content in the mixtures, the CF moved closer to the correspondent endmember (see Figure 3). This behaviour is not linear, and it is influenced by the presence of the second maximum of the Mg-GN, which separates the RB0 from the rest of the RB minima (see Figures 1 and 2).

RBs 1–4 were always present (apart from in the CaS spectra), giving a clear indication of the mafic components up to at least 60% CaS, conversely from CF. RB1 and RB3 were those moving more systematically from the wavenumber of Mg-GN up to the wavenumbers of RB1* and RB4* with increases to both the percentage of CaS and the temperature (Figure 4). RB1 moved from 1001 to 1018 cm^{-1}, increasing the wavenumber for Mg-GN to 60% CaS (Figure 5a,c), whereas RB3 moved from 928 to 910 cm^{-1}, decreasing the wavenumber (Figure 5b,d). RB2 instead was strongly diagnostic, since it showed a weak shift (Figure 4), 8 cm^{-1} lower than that which appears for Mg-GN and for all the mixtures. In fact, it showed the highest shift with the temperature for the endmembers itself (from 959 cm^{-1} at 375 K up to 951 cm^{-1} at 675 K, see Table 1), and it showed the highest shifts with respect to all the samples at the highest temperature (from 951 cm^{-1} for Mg-GN up to 959 cm^{-1} for the 60% CaS; see Table 2) (Figure 5a,c). RB4 displayed a trend towards lower wavenumbers, since it moves from 876 cm^{-1} to 862 cm^{-1} increasing the CaS percentage (Figure 5b,d), despite the CaS is at ~1030 cm^{-1}. The wider shift is present for the 60% CaS (the sample with the mafic material at lower wavenumber) up to RB4*, for all the temperatures. This is mainly attributable to the influence of RB5 in CaS (Figures 1 and 2, Tables 1 and 2), which is at 833–794 cm^{-1}, varying the temperature.

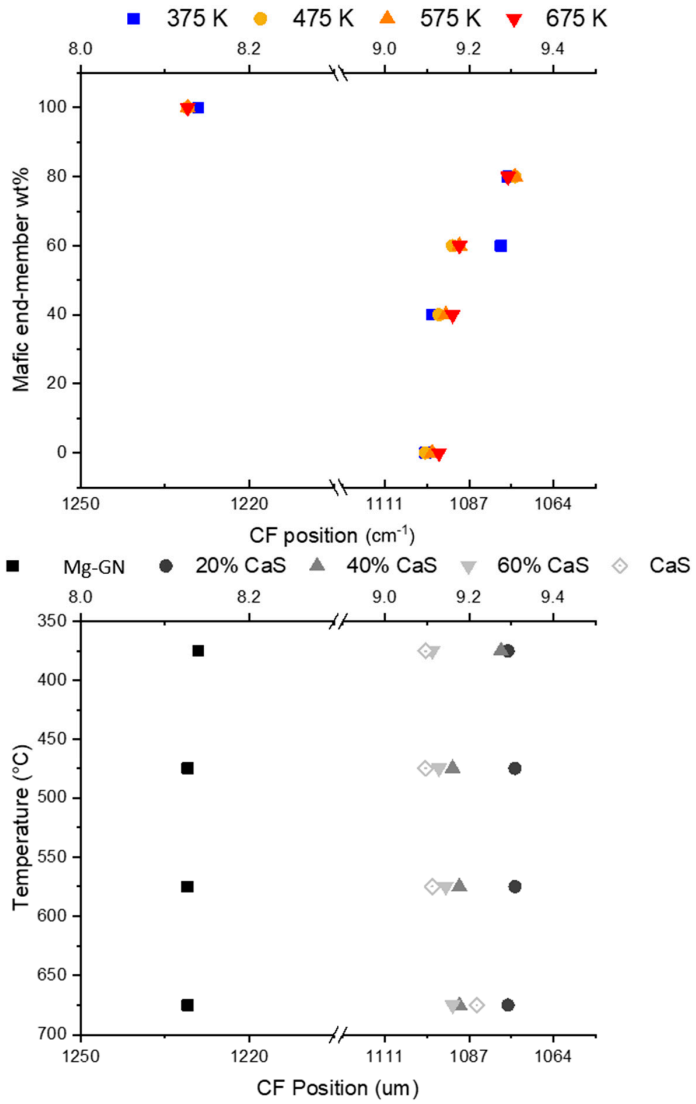

Figure 3. Variations in the position of the CF plotted against fraction of Mg-GN (**top**) and temperature (**bottom**).

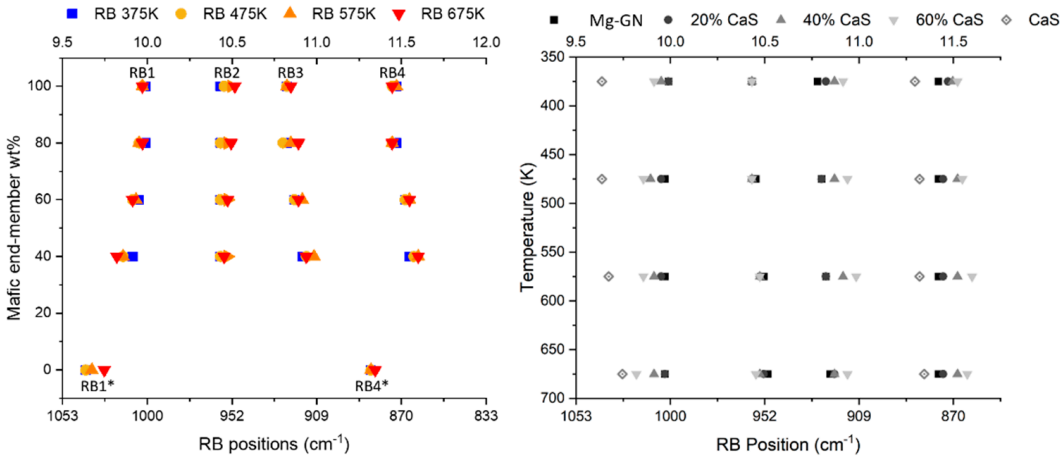

Figure 4. The positions of the RBs plotted against the fraction of Mg=−GN (**left**) and temperature (**right**).

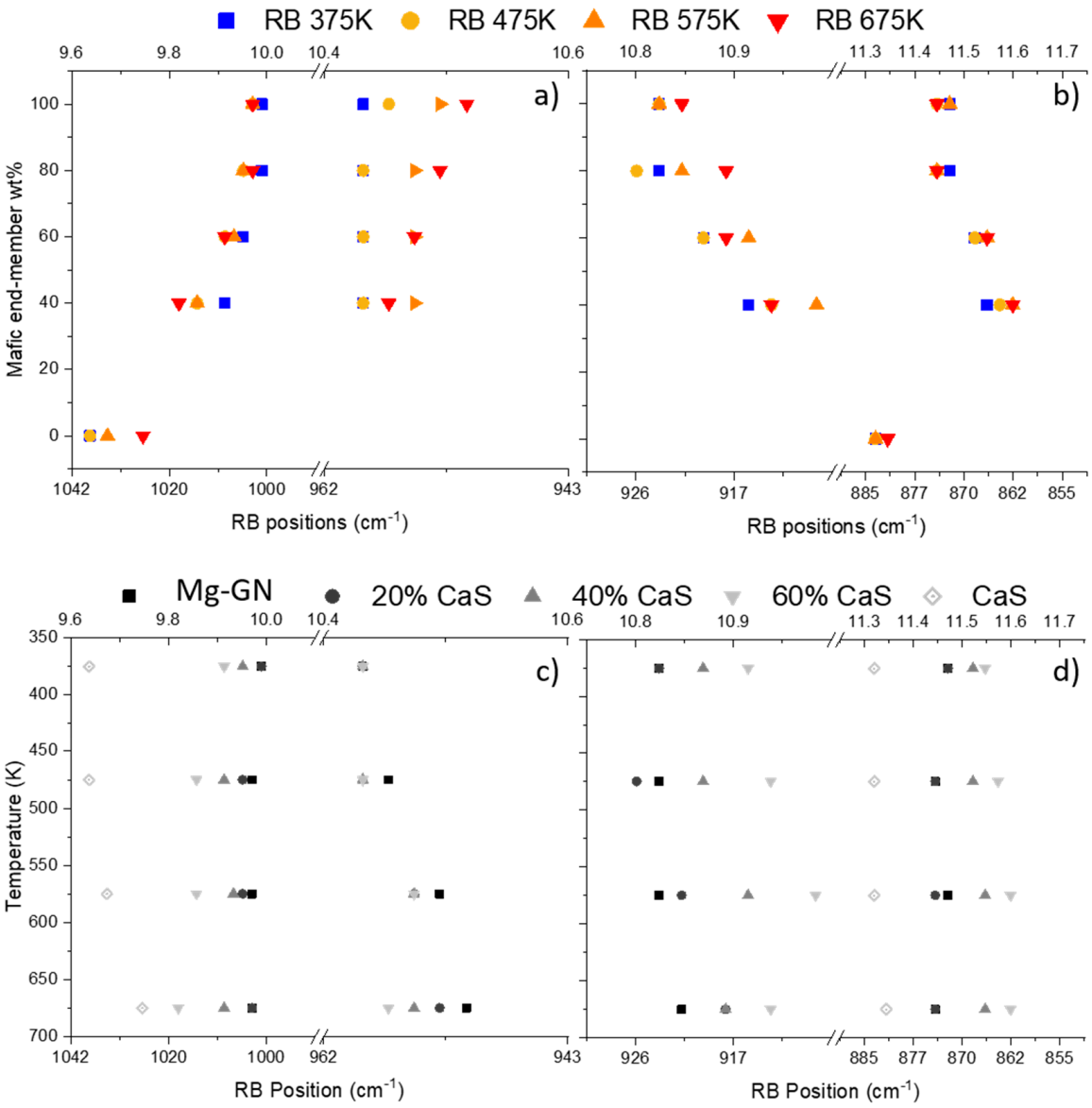

Figure 5. The position of RBs plotted against the fraction of Mg-GN (**top**) and temperature (**bottom**), highlighted for RBs 1,2 (**a**,**c**) and RBs 3,4 (**b**,**d**).

In Figure 6, the spectral contrast (i.e., the differences between the CF emissivity and the absorption–minima emissivity; see also [46]) of RBs 1–4 is compared to temperature (upper panel) and composition (lower panel). Interestingly, the spectral contrast showed a very similar behaviour for all four RBs. It showed the highest values for the two end-members and then, in general, moved from 60% CaS, 40% CaS and 20% CaS, for which it showed the lower spectral contrast (Figure 6 top panel). Moreover, the spectral contrast seemed to increase with increasing temperature, as it appears in Figure 2. Nevertheless, the increase with temperature was evident for the two endmembers for all the 4 RBs (Figure 6, below panel and Table 3), whereas it was not for the mixtures, showing how the mineralogical variations (in terms of percentage) of each endmember affect the spectral contrast too. Moreover, on average between the different temperatures, the value of spectral contrast from 20% CaS up to 60% CaS was almost identical. The variations in RB2 and RB3 were negligible (from 0.056 ± 0.015 up to 0.065 ± 0.014, and from 0.047 ± 0.016 up to 0.060 ± 0.016, respectively), whereas the slight increase for RB1 and RB4 (from 0.054 ± 0.011 up to 0.080 ± 0.008, and from 0.028 ± 0.016 up to 0.061 ± 0.017, respectively) was affected by the intensity of the CaS absorption (Figure 6, below panel).

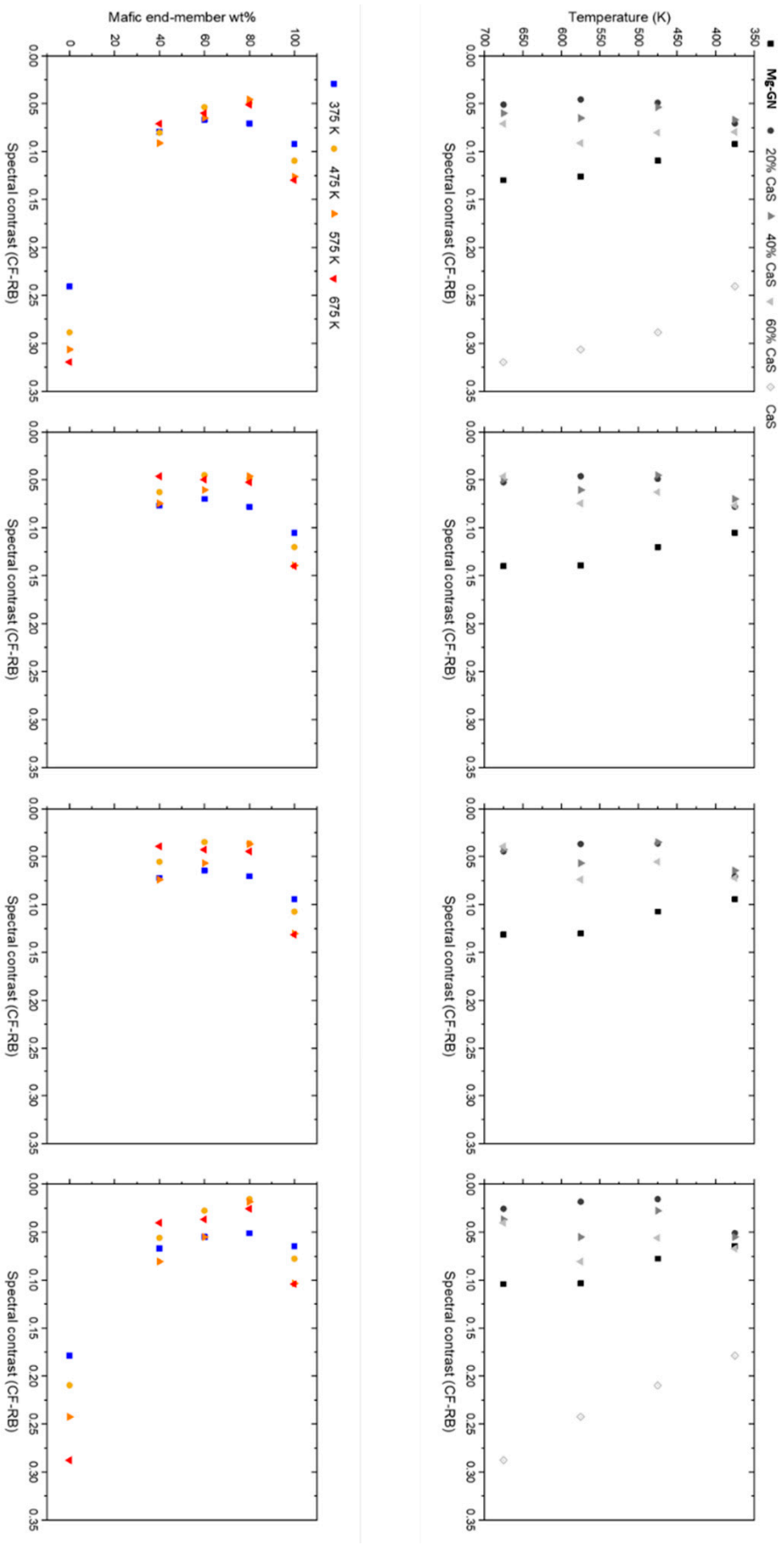

Figure 6. The spectra plotted against the temperature (**top**) and the fraction of Mg-GN (**bottom**).

4. Discussion

Oldhamite has been reported in meteorites [52,53], and its presence is also suggested for the Hermean surface (e.g., [1]). Moreover, oldhamite stability is demonstrated in highly reducing conditions [52] and at high temperatures [22]. On Mercury's surface, CaS is possibly mixed with volcanic bedrock with mafic mineralogy enriched in Mg. Here, we analysed the MidIR emissivity properties of potential mixtures of oldhamite and a Mg-rich GN (Figures 1 and 2), to investigate the future possibility of identifying them from BepiColombo remote sensing data.

The CF position had distinct values between the Mg-GN and the CaS, and it moved closer to the CF position of the CaS even for the 20% CaS sample (Figure 3). This clearly indicates that relatively low abundance of CaS within the regolith could be identified using TIR measurements. The presence of a secondary maximum in the Mg-rich mafic endmember within the Reststrahlen minima at wavenumber ~1070 cm^{-1}, lower than the CF position of CaS, affected the shift. In fact, the CF showed a lower wavenumber position for the 20% CaS, and the CF wavenumber increased for higher CaS abundances. This could also help to distinguish, with MERTIS data, regions with low CaS with respect to those dominated by CaS.

The shift attributable to the temperature for each sample was much lower (~3 cm^{-1}), indicating that any CF shift detected via MERTIS should be attributed to compositional variation. Nevertheless, the CF of CaS showed a shift of 14 cm^{-1}, mainly moving from 575 K to 675 K (Tables 1 and 2 and Figure 3). This shift, attributable to temperature, could also be detected via MERTIS, which has a resolution of 90 nm [35], which means a variation from 5 to 20 cm^{-1} [46].

Moving to lower wavenumbers, the RBs of mafic material showed 5 minima (RBs 0, 1, 2, 3 and 4) with four of them clearly identifiable also on the mixture spectra (RBs 1, 2, 3 and 4). RBs appeared at lower wavenumbers with respect to the CF. Three different minima are present in the CaS, closer to the position in mafic endmembers, reported as RBs 1*, 4* and 5. RBs 1, 2, 3 and 4 are identifiable for each sample bearing Mg-GN and for all the temperatures considered. This clearly indicates that the composition of the volcanic rocks present in the regolith could be clearly distinguished with RBs even for high abundance (at least 60%) of CaS, unlike the CF.

The positions of RBs 1, 3 and 4 were affected by the increasing abundance of CaS, with RB1 moving towards RB1* and RB3 and RB4 shifting towards RB4* and RB5, respectively. The shifts of the RBs seems to have been affected by the CaS's properties. CaS has an expansion coefficient (αV) of 4.03×10^{-5} K^{-1} [22], which is higher than those related to the main silicates present on a typical volcanic rock, e.g., 2.2×10^{-5} K^{-1} for a plagioclase [54] or 2.7×10^{-5} K^{-1} for a clinopyroxene [41]. Similar to what was evidenced in [46], this behaviour seems to confirm that the minerals with higher expansion coefficient also drive the main RB shifts in the mixtures.

RB2 showed a relative smaller shift (from 959 to 951 cm^{-1} from 375 K up to 675 K, for Mg-GN); this indicates that RB2 was less influenced, with respect to the other RBs, by mineral mixing with CaS (Figure 4). Though RB2 showed a peculiar variation in function of the temperature, at 375 K, all the spectra had the same absorption position, which shows a shift towards lower wavenumber increasing the Mg-GN abundance at higher temperature (Figure 5), similar to those observed in [46].

The spectra showed, in general, decreasing emissivity with increasing temperature, in particular at wavenumbers higher than the CF (Figure 2), and the RBs seem to have had the same behaviour. Once we highlighted the behaviour of the apparent intensity (see Table 3 and Figure 6), the RBs became deeper only for the two endmembers Mg-GN and CaS spectra, with RBs deepening with increasing temperature, whereas within mixtures, the relative intensity of RBs is strongly reduced in 60% CaS, since for 20% CaS and 40% CaS it is negligeable. Interestingly, this demonstrates that varying the temperatures and taking into account endmembers with the same particle sizes, the variation in the spectral contrast is more effective for CaS than Mg-GN.

5. Conclusions

TIR measurements of the two endmembers considered in this work support the probable capability to detect the presence of oldhamite on the surface of Mercury with the BepiColombo MERTIS instrument, even if oldhamite is mixed with a Mg-enriched volcanic regolith. Endmembers and mixtures, in fact, show very different spectral properties, having CF at different wavenumbers and having different RBs. Furthermore, it is evident that certain features are predominantly influenced by one endmember or the other. In several cases, the variations in mineral abundance have a more pronounced impact than temperature shifts on these features.

In particular, the CF was strongly driven by the CaS; therefore, the 20% CaS mixture already showed a CF at wavenumbers closer to the CaS end-memeber. However, an interesting shift is also associated to the maxima between RB0 and RB1 in the Mg-GN. This shift is towards lower wavenumbers with respect to the two endmembers, which may help the oldhamite interpretation. In fact, a small shift of the CF from the expected position for the oldhamite could give an indication of a relatively low amount of oldhamite within a specific pixel.

Conversely, for all the mixtures investigated here, the RBs indicate the presence of the mafic Mg-GN endmember. Nevertheless, at least for three of them, RBs 1, 3 and 4, the presence of the CaS was effective, with shifts that went towards RB1*, RB4* and RB5, whereas RB2 showed a very reduced shift, which is important to quantify Mg-GN composition. Moreover, RB2 could permit us to differentiate regions where oldhamite can be present with respect to regions where it is negligible.

Emissivity as a function of temperature was mainly evident for the endmembers, with an RB–CF spectral contrast that increased with the temperature. In the mixtures, lower spectral contrast values occurred even if an asymmetrical variation with respect to the composition change was evident, indicating that oldhamite spectra show more intense absorption in the RB spectral region with respect to Mg-GN.

MERTIS laboratory performance showed signal-to-noise ratios greater than 200 in the 1000–1200 cm^{-1} range, indicating a noise level lower than 0.5% [55], and conservatively 1% for the entire spectral range [35]. Such performance of the instrument will permit us to demonstrate several of the features discussed here. Moreover, considering the spectral resolution of the instrument, the most prominent and diagnostic shifts due to the composition effects, also within the mixtures, will be highlighted, not only for the CF but also for RBs 1 and 3, with RB4's maximum shift closer to the resolution, whereas the shifts due to the temperature within each feature are mainly lower than the spectral resolution, even if for some features, and in particular, for RB5, the temperature effects should be present.

We suggest that future studies should explore the range from 20% CaS down to 0% CaS (mafic endmember) to better highlight the variation in the spectra for lower CaS abundance than those explored in this work. In particular, this is expected to retrieve possible correlation lines for the CF, which could be pivotal to detect and quantify the CaS within the hollows as well as in the regolith.

Author Contributions: Conceptualization, C.C., A.M. (Alessandro Maturilli) and G.S.; Methodology, C.C., S.F., A.M. (Alessandro Maturilli) and G.S.; Formal Analysis, C.C., G.S. and S.F.; Investigation, C.C., G.S. and S.F.; Resources, C.C., M.S., A.M. (Alessandro Maturilli), A.S., A.M. (Alessandra Montanini) and J.H.; Data Curation, A.M. (Alessandro Maturilli), C.C. and G.S.; Writing—Original Draft Preparation, C.C.; Writing—Review & Editing, C.C., S.F., M.S., A.S. and A.M. (Alessandra Montanini); Supervision, J.H. Funding Acquisition, G.S. and C.C. All authors have read and agreed to the published version of the manuscript.

Funding: This work was supported by TNA Europlanet 2020 RI, grant No 654208, funded from the European Union's Horizon 2020 research and innovation programme. CC also want to thank the Italian Space Agency (SIMBIO-SYS project within ASI-INAF agreement 2017-47-H.0).

Data Availability Statement: Data available on request due to restrictions related to DLR database.

Acknowledgments: Authors want to thank two anonymous reviewers and the third, Larry Nittler, that help to improve the manuscript.

Conflicts of Interest: The authors declare no conflicts of interest.

References

1. Nittler, L.R.; Starr, R.D.; Weider, S.Z.; McCoy, T.J.; Boynton, W.V.; Ebel, D.S.; Ernst, C.M.; Evans, L.G.; Goldsten, J.O.; Hamara, D.K.; et al. The major-element composition of Mercury's surface from MESSENGER X-ray spectrometry. *Science* **2011**, *333*, 1847–1850. [CrossRef] [PubMed]
2. Schlemm, C.E.; Starr, R.D.; Ho, G.C.; Bechtold, K.E.; Hamilton, S.A.; Boldt, J.D.; Boynton, W.V.; Bradley, W.; Fraeman, M.E.; Gold, R.E.; et al. The X-Ray Spectrometer on the MESSENGER spacecraft. *Space Sci. Rev.* **2007**, *131*, 393–415. [CrossRef]
3. Goldsten, J.O.; Rhodes, E.A.; Boynton, W.V.; Feldman, W.C.; Lawrence, D.J.; Trombka, J.I.; Smith, D.M.; Evans, L.G.; White, J.; Madden, N.W.; et al. The MESSENGER Gamma-Ray and Neutron Spectrometer. *Space Sci. Rev.* **2007**, *131*, 339–391. [CrossRef]
4. Peplowski, P.N.; Evans, L.G.; Hauck, S.A.; McCoy, T.J.; Boynton, W.V.; Gillis-Davis, J.J.; Ebel, D.S.; Goldsten, J.O.; Hamara, D.K.; Lawrence, D.J.; et al. Radioactive elements on Mercury's surface from MESSENGER: Implications for the planet's formation and evolution. *Science* **2011**, *333*, 1850–1852. [CrossRef] [PubMed]
5. McClintock, W.E.; Lankton, M.R. The Mercury atmospheric and surface composition spectrometer for the MESSENGER mission. *Space Sci. Rev.* **2007**, *131*, 481–521. [CrossRef]
6. McClintock, W.E.; Izenberg, N.R.; Holsclaw, G.M.; Blewett, D.T.; Domingue, D.L.; Head, J.W., III; Helbert, J.; McCoy, T.J.; Murchie, S.L.; Robinson, M.S.; et al. Spectroscopic observations of Mercury's surface reflectance during MESSENGER's first Mercury flyby. *Science* **2008**, *321*, 62–65. [CrossRef]
7. Hawkins, S.E.; Boldt, J.D.; Darlington, E.H.; Espiritu, R.; Gold, R.E.; Gotwols, B.; Grey, M.P.; Hash, C.D.; Hayes, J.R.; Jaskulek, S.E.; et al. The Mercury Dual Imaging System on the MESSENGER Spacecraft. *Space Sci. Rev.* **2007**, *131*, 247–338. Available online: https://link.springer.com/chapter/10.1007/978-0-387-77214-1_9 (accessed on 23 October 2007). [CrossRef]
8. Robinson, M.S.; Murchie, S.L.; Blewett, D.T.; Domingue, D.L.; Hawkins, S.E., III; Head, J.W.; Holsclaw, G.M.; McClintock, W.E.; McCoy, T.J.; McNutt, R.L.; et al. Reflectance and color variations on Mercury: Regolith processes and compositional heterogeneity. *Science* **2008**, *321*, 66–69. [CrossRef]
9. Vilas, F.; Domingue, D.L.; Helbert, J.; D'Amore, M.; Maturilli, A.; Klima, R.L.; Stockstill-Cahill, K.R.; Murchie, S.L.; Izenberg, N.R.; Blewett, D.T.; et al. Mineralogical indicators of Mercury's hollows composition inMESSENGER color observations. *Geophys. Res. Lett.* **2016**, *43*, 1450–1456. [CrossRef]
10. Helbert, J.; Maturilli, A.; D'Amore, M. Visible and near-infrared reflectance spectra of thermally processed synthetic sulfides as a potential analog for the hollow forming materials on Mercury. *Earth Planet. Sci. Lett.* **2013**, *369*, 233–238. [CrossRef]
11. Lucchetti, A.; Pajola, M.; Galluzzi, V.; Giacomini, L.; Carli, C.; Cremonese, G.; Marzo, G.A.; Ferrari, S.; Massironi, M.; Palumbo, P. Mercury hollows as remnants of original bedrock materials and devolatilization processes: A spectral clustering and geomorphological analysis. *J. Geophys. Res. Planets* **2018**, *123*, 2365–2379. [CrossRef]
12. Blewett, D.T.; Chabot, N.L.; Denevi, B.W.; Ernst, C.M.; Head, J.W.; Izenberg, N.R.; Murchie, S.L.; Solomon, S.C.; Nittler, L.R.; McCoy, T.J.; et al. Hollows on Mercury: MESSENGER evidence for geologically recent volatile-related activity. *Science* **2011**, *333*, 1856–1859. [CrossRef] [PubMed]
13. Blewett, D.T.; Vaughan, W.M.; Xiao, Z.; Chabot, N.L.; Denevi, B.W.; Ernst, C.M.; Helbert, J.; D'Amore, M.; Maturilli, A.; Head, J.W.; et al. Mercury's hollows: Constraints on formation and composition from analysis of geological setting and spectral reflectance. *J. Geophys. Res. Planets* **2013**, *118*, 1013–1032. [CrossRef]
14. Weider, S.Z.; Nittler, L.R.; Starr, R.D.; McCoy, T.J.; Stockstill-Cahill, K.R.; Byrne, P.K.; Denevi, B.W.; Head, J.W.; Solomon, S.C. Chemical heterogeneity on Mercury's surface revealed by the MESSENGER X-Ray Spectrometer. *J. Geophys. Res.* **2012**, *117*, E00L05. [CrossRef]
15. Head, J.W.; Murchie, S.L.; Prockter, L.M.; Solomon, S.C.; Chapman, C.R.; Strom, R.G.; Watters, T.R.; Blewett, D.T.; Gillis-Davis, J.J.; Fassett, C.I.; et al. Volcanism on Mercury: Evidence from the first MESSENGER flyby for extrusive and explosive activity and the volcanic origin of plains. *Earth Planet. Sci. Lett.* **2009**, *285*, 227–242. [CrossRef]
16. Thomas, R.J.; Rothery, D.A.; Conway, S.J.; Anand, M. Mechanisms of explosive volcanism on Mercury: Implications from its global distribution and morphology. *J. Geophys. Res. Planets* **2014**, *119*, 2239–2254. [CrossRef]
17. Besse, S.; Doressoundiram, A.; Barraud, O.; Griton, L.; Cornet, T.; Crego, C.M.; Varatharajan, I.; Helbert, J. Spectral properties and physical extent of pyroclastic deposits on mercury: Variability within selected deposits and implications for explosive volcanism. *J. Geophys. Res Planets* **2020**, *125*, e2018JE005879. [CrossRef]
18. Galiano, A.; Capaccioni, F.; Filacchione, G.; Carli, C. Spectral identification of pyroclastic deposits on Mercury with MASCS/MESSENGER data. *Icarus* **2022**, *388*, 115233. [CrossRef]
19. Kerber, L.; Head, J.W.; Blewett, D.T.; Solomon, S.C.; Wilson, L.; Murchie, S.L.; Robinson, M.S.; Denevi, B.W.; Domingue, D.L. The global distribution of pyroclastic deposits on Mercury: The view from MESSENGER flybys 1–3. *Planet. Spac. Sci.* **2011**, *59*, 1895–1909. [CrossRef]
20. Namur, O.; Charlie, B.; Holtz, F.; Carter, C.; McCammon, C. Sulfur solubility in reduced mafic silicate melts: Implications for the speciation and distribution of sulfur on Mercury. *EPSL* **2016**, *448*, 102–114. [CrossRef]

21. Varatharajan, I.; Maturilli, A.; Helbert, J.; Alemanno, G.; Hiesinger, H. Spectral behavior of sulfides in simulated daytime surface conditions of Mercury: Supporting past (MESSENGER) and future missions (BepiColombo). *Earth Planet. Sci. Lett.* **2019**, *520*, 127–140. [CrossRef]
22. Barbaro, A.; Zorzi, F.; Lorenzetti, A.; Ferrari, S.; Tubaro, C.; Nestola, F. Thermal expansion of Oldhamite, CaS: Implication for the surface of Mercury. *Icarus* **2023**, *401*, 115629. [CrossRef]
23. Namur, O.; Charlier, B. Silicate mineralogy at the surface of Mercury. *Nat. Geosci.* **2017**, *10*, 9–13. [CrossRef]
24. Stockstill-Cahill, K.R.; McCoy, T.J.; Nittler, L.R.; Weider, S.Z.; Hauck, S.A., II. Magnesium-rich crustalcompositions on Mercury: Implications for magmatism from petrologic modeling. *J. Geophys. Res.* **2012**, *117*, E00L15. [CrossRef]
25. Charlier, B.; Grove, T.L.; Zuber, M.T. Phase equilibria of ultramafic compositions on Mercury and the origin of the compositional dichotomy. *Earth Planet. Sci. Lett.* **2013**, *363*, 50–60. [CrossRef]
26. Vander Kaaden, K.E.; McCubbin, F.M.; Nittler, L.R.; Peplowski, P.N.; Weider, S.Z.; Frank, E.A.; McCoy, T.J. Geochemistry, mineralogy, and petrology of boninitic and komatiitic rocks on the mercurian surface: Insights into the mercurian mantle. *Icarus* **2017**, *285*, 155–168. [CrossRef]
27. Weider, S.Z.; Nittler, L.R.; Starr, R.D.; McCoy, T.J.; Solomon, S.C. Variations in the abundance of iron on Mercury's surface from MESSENGER x-ray spectrometer observations. *Icarus* **2014**, *235*, 170–186. [CrossRef]
28. Klima, R.L.; Izenberg, N.R.; Holsclaw, G.M.; Helbert, J.; D'Amore, M.; McClintock, W.E.; Solomon, S.C. Visible to near-infrared hyperspectral measurements of mercury: Challenges for deciphering surface mineralogy. In Proceedings of the 6th Workshop on Hyperspectral Image and Signal Processing: Evolution in Remote Sensing (WHISPERS), Lausanne, Switzerland, 24–27 June 2014; pp. 1–4. [CrossRef]
29. Hamilton, V.E. Thermal infrared (vibrational) spectroscopy of Mg–Fe olivines: A review and applications to determining the composition of planetary surfaces. *Geochemistry* **2010**, *70*, 7–33. [CrossRef]
30. Helbert, J.; Nestola, F.; Ferrari, S.; Maturilli, A.; Massironi, M.; Redhammer, G.J.; Capria, M.T.; Carli, C.; Capaccioni, F.; Bruno, M. Olivine thermal emissivity under extreme temperature ranges: Implication for Mercury surface. *Earth Planet. Sci. Lett.* **2013**, *371–372*, 252–257. [CrossRef]
31. Farmer, V.C. *The Infrared Spectra of Minerals*; Mineralogical Society of Great Britain and Ireland: London, UK, 1974; pp. 1–540.
32. Christensen, P.R.; Bandfield, J.L.; Hamilton, V.E.; Howard, D.A.; Lane, M.D.; Piatek, J.L.; Ruff, S.W.; Stefanov, W.L. A thermal emission spectral library of rock-forming minerals. *JGR* **2000**, *105*, 9735–9739. [CrossRef]
33. Nash, D.B.; Salisbury, J.W. Infrared reflectance spectra (2.2–15 mm) of plagioclase feldspars. *Geophys. Res. Lett.* **1991**, *18*, 1151–1154. [CrossRef]
34. Milam, K.A.; McSween, H.Y., Jr.; Christensen, P.R. Plagioclase compositions derived from thermal emis-sion spectra of compositionally complex mixtures: Implications for Martian feldspar mineralogy. *J. Geophys. Res.* **2007**, *112*, E10005. [CrossRef]
35. Reitze, M.P.; Weber, I.; Morlok, A.; Hiesinger, H.; Bauch, K.E.; Stojic, A.N.; Helbert, J. Mid-infrared spectros-copy of crystalline plagioclase feldspar samples with various Al, Si order and implications for remote sensing of Mercury and other terrestrial Solar System objects. *Earth Planet. Sci. Lett.* **2021**, *554*, 116697. [CrossRef]
36. Vander Kaaden, K.E.; McCubbin, F.M. The origin of boninites on Mercury: An experimental study of the northern volcanic plains lavas. *Geochim. Et Cosmochim. Acta* **2016**, *173*, 246–263. [CrossRef]
37. Peplowski, P.N.; Evans, L.G.; Stockstill-Cahill, K.R.; Lawrence, D.J.; Goldsten, J.O.; McCoy, T.J.; Nittler, L.R.; Solomon, S.C.; Sprague, A.L.; Starr, R.D.; et al. Enhanced sodium abundance in Mercury's north polar region revealed by the MESSENGER Gamma-Ray spectrometer. *Icarus* **2014**, *228*, 86–95. [CrossRef]
38. Capaccioni, F.; Filacchione, G.; Piccioni, G.; Dami, M.; Tommasi, L.; Barbis, A.; Ficai-Veltroni, I. Pre-Launch Calibrations of the Vis-IR Hyperspectral Imager (VIHI) onboard BepiColombo, the ESA Mission to Mercury. In *Proceedings of the SPIE*; Society of Photo-Optical Instrumentation Engineers (SPIE) Conference Series; SPIE: Bellingham, WA, USA, 2013; Volume 8867, p. 886704. [CrossRef]
39. Cremonese, G.; Capaccioni, F.; Capria, M.T.; Doressoundiram, A.; Palumbo, P.; Vincendon, M.; Massironi, M.; Debei, S.; Zusi, M.; Altieri, F.; et al. SIMBIO-SYS; scientific cameras and spectrometer for the BepiColombo Mission. *Space Sci. Rev.* **2020**, *216*, 75. [CrossRef]
40. Hiesinger, H.; Helbert, J.; Alemanno, G.; Bauch, K.E.; D'amore, M.; Maturilli, A.; Morlok, A.; Reitze, M.P.; Stangarone, C.; Stojic, A.N.; et al. Studying the Composition and Mineralogy of the Hermean Surface with the Mercury Radiometer and Thermal Infrared Spectrometer (MERTIS) for the BepiColombo Mission: An Update. *Space Sci. Rev.* **2020**, *216*, 110. [CrossRef]
41. Ferrari, S.; Nestola, F.; Massironi, M.; Maturilli, A.; Helbert, J.; Alvaro, M.; Domeneghetti, M.C.; Zorzi, F. In-situ high-temperature emissivity spectra and thermal expansion of C2/c pyroxenes: Implications for the surface of Mercury. *Am. Mineral.* **2014**, *99*, 786–792. [CrossRef]
42. Maturilli, A.; Helbert, J.; St. John, J.M.; Head, J.W., III; Vaughan, W.M.; D'Amore, M.; Gottschalk, M.; Ferrari, S. Komatiites as Mercury surface analogues: Spectral measurements at PEL. *Earth Planet. Sci. Lett.* **2014**, *398*, 58–65. [CrossRef]
43. Carli, C.; Capaccioni, F.; Maturilli, A.; Ammannito, E.; Ferrari, S.; Nestola, F.; Helbert, J.; Massironi, M.; Sgavetti, M.; Serventi, G. Studying basalts spectra in the VNIR and MidIR: What we could learn integrating data from VIHI and MERTIS the spectrometers onboard BepiColombo. In Proceedings of the EGU General Assembly, Vienna, Austria, 22–27 April 2012; p. 6099.

44. Carli, C.; Serrano, L.M.; Maturilli, A.; Massironi, M.; Capaccioni, F.; Helbert, J. VNIR and TIR spectra of terrestrial komatiites possibly analogues of some hermean terrain compositions. In Proceedings of the 44th Lunar and Planetary Science Conference, The Woodlands, TX, USA, 18–22 March 2013. Abstract 1923.
45. Maturilli, A.; Helbert, J.; Varatharajan, I.; D'Amore, M. Emissivity Spectra of Mercury Analogues under Mercury Pressure and Temperature Conditions. *EPSC* **2017**, *11*, EPSC2017-610.
46. Ferrari, S.; Maturilli, A.; Carli, C.; D'Amore, M.; Helbert, J.; Nestola, F.; Hiesinger, H. Thermal infrared emissivity of felsic-rich to mafic-rich analogues of hot planetary regoliths. *Earth Planet. Sci. Lett.* **2020**, *534*, 116089. [CrossRef]
47. Secchiari, A.; Montanini, A.; Bosch, D.; Macera, P.; Cluzel, D. The contrasting geochemical message from the New Caledonia gabbronorites: Insights on depletion and contamination processes of the sub-arc mantle in a nascent arc setting. *Contrib. Mineral. Petrol.* **2018**, *173*, 66. [CrossRef]
48. Bruschini, E.; Carli, C.; Buellet, A.-C.; Vincendon, M.; Capaccioni, F.; Ferrari, M.; Vetere, F.; Secchiari, A.; Perugini, D.; Montanini, A. VNIR reflectance spectra of silicate-graphite mixtures: The effect of graphite content and particle size. *Icarus* **2022**, *378*, 114950. [CrossRef]
49. Lyon, R.J.P. *Evaluation of Infrared Spectrophotometry for Compositional Analysis of Lunar and Planetary Soils*; No. NASA-TN-D1871; National Aeronautics and Space Administration: Washington, DC, USA, 1963.
50. Salisbury, J.W.; Walter, L.S. Thermal infrared (2.5–13.5 μm) spectroscopic remote sensing of igneous rock types on particulate planetary surfaces. *J. Geph. Res.* **1989**, *94*, 9192–9202. [CrossRef]
51. Cooper, B.L.; Salisbury, J.W.; Killen, R.M.; Potter, A.E. Midinfrared spectral features of rocks and their powders. *J. Geophys. Res.* **2022**, *107*, 5017. [CrossRef]
52. Liu, Y.; Chou, I.-M.; Chen, J.; Wu, N.; Li, W.; Bagas, L.; Ren, M.; Liu, Z.; Mei, S.; Wang, L. Oldhamite: A new link in upper mantle for C–O–S–Ca cycles and an indicator for planetary habitability. *Natl. Sci. Rev.* **2023**, *10*, nwad159. [CrossRef]
53. Carli, C.; Barbaro, A.; Murri, M.; Domeneghetti, M.C.; Langone, A.; Bruschini, E.; Stephant, A.; Alvaro, M.; Stefani, S.; Cuppone, T.; et al. Al Huwaysah 010: The most reduced brachinite, so far. *Meteorit. Planet. Sci.* **2023**, *6*, 855–874. [CrossRef]
54. Tribaudino, M.; Angel, R.J.; Cámara, F.; Nestola, F.; Pasqual, D.; Margiolaki, I. Thermal expansion of plagioclase feldspars. *Contrib. Mineral. Petrol.* **2010**, *160*, 899–908. [CrossRef]
55. D'Amore, M.; Helbert, J.; Maturilli, A.; Varatharajan, I.; Ulmer, B.; Säuberlich, T.; Berlin, R.; Peter, G.; Hiesinger, H.; Martinez, S.; et al. Data Processing of the Mercury Radiometer and Thermal Infrared Imaging Spectrometer (MERTIS) onboard Bepi Colombo. In *Infrared Remote Sensing and Instrumentation XXVI*; Strojnik, M., Kirk, M.S., Eds.; SPIE: Bellingham, WA, USA, 2018; p. 16.